Inorg. Chem. **2009**, *48*, 3982−3992

Exploring the Ground and Excited State Potential Energy Landscapes of the Mixed-Valence Biferrocenium Complex

Ryan G. Hadt and Victor N. Nemykin*

Department of Chemistry & Biochemistry, University of Minnesota Duluth, Duluth, Minnesota 55812

Received September 19, 2008

Density functional theory (DFT) and time-dependent DFT (TDDFT) have been used to explore the potential energy landscapes in the class II (in Robin and Day classification) mixed-valence biferrocenium mono-cation (**BF**$^+$) in an effort to evaluate factors affecting optical and thermal intramolecular electron transfer rates. Both energy- and spectroscopy-based benchmarks were used to explore the adiabatic potential energy surfaces (PESs) of the mixed-valence **BF**$^+$ cation along with the optimization of appropriate ground-, excited-, and transition-state geometries. The calculation of Mössbauer isomer shifts and quadrupole splittings, UV−vis excitation energies, and the electronic coupling matrix element, H_{ab}, corroborate the PES analyses. The adiabatic electron transfer pathway is also analyzed with respect to several possible vibronic coordinates. The degree of the electronic coupling between iron sites, the value of H_{ab}, and the nature of the electron transfer pathway correlate with the amount of Hartree−Fock exchange involved in the DFT calculation with hybrid (∼20% of Hartree−Fock exchange) methods providing the best agreement between theory and experiment. DFT (B3LYP) predicted values of H_{ab} (839, 1085, and 1265 cm^{-1}) depend on the computational method and are in good agreement with experimental data.

Introduction

Multinuclear-containing compounds exhibiting strong short- or long-range metal−metal coupling represent an important class of metallocomplexes.[1] These molecules are interesting both from practical (i.e., molecular electronics), as well as fundamental (i.e., magnetic coupling, multiredox processes, and unpaired electron density migration), points of view.[2−5] An additional interest lies in the formation of mixed-valence (MV) states, an intriguing phenomenon occurring in polynuclear transition-metal complexes, particularly those with ferrocene substituents.[4] The formation of MV complexes in bisferrocenes was discovered a long time ago, and the influence of different factors on the formation and stability of MV states has been intensely investigated.[6−14] Depending on the specific structure, MV bisferrocenes can behave as class II (localized) or class III (delocalized) compounds in the Robin and Day classification.[15]

Traditionally, the Hush method for the analysis of experimental data, specifically of properties of the intervalence charge transfer (IVCT) band, is used for the evaluation of the H_{ab} coupling element by the majority of synthetic chemists.[16] A more descriptive analysis of the intramolecular electron transfer characteristics in MV compounds, however,

* To whom correspondence should be addressed. E-mail: vnemykin@d.umn.edu.

(1) (a) Kaim, W.; Lahiri, G. K. *Angew. Chem., Int. Ed.* **2007**, *46*, 1778. (b) Kaim, B.; Sarkar, B. *Coord. Chem. Rev.* **2007**, *251*, 584. (c) Chisholm, M. H.; Patmore, N. J. *Acc. Chem. Res.* **2007**, *40*, 19. (d) Solomon, E. I.; Sarangi, R.; Woertink, J. S.; Augustine, A. J.; Yoon, J.; Ghosh, S. *Acc. Chem. Res.* **2007**, *40*, 581.
(2) Miller, J. S.; Epstein, A. J. *Angew. Chem., Int. Ed. Engl.* **1994**, *33*, 385.
(3) Epstein, A. J.; Miller, J. S. *Synth. Met.* **1996**, *80*, 231.
(4) Barlow, S.; O'Hare, D. *Chem. Rev.* **1997**, *97*, 637.
(5) Barlow, S. *Inorg. Chem.* **2001**, *40*, 7047.
(6) Cowan, D. O.; Kaufman, F. *J. Am. Chem. Soc.* **1970**, *92*, 6198.
(7) Cowan, D. O.; Kaufman, F. *J. Am. Chem. Soc.* **1970**, *92*, 219.
(8) Morrison, W. H., Jr.; Hendrickson, D. N. *Chem. Phys. Lett.* **1973**, *22*, 119.
(9) Morrison, W. H.; Krogsrud, S.; Hendrickson, D. N. *Inorg. Chem.* **1973**, *12*, 1998.
(10) Morrison, W. H., Jr. ; Hendrickson, D. N. *Inorg. Chem.* **1975**, *14*, 2331.
(11) Dong, T. Y.; Hendrickson, D. N. *Bull. Inst. Chem., Acad. Sinica* **1987**, *34*, 67.
(12) Tolbert, L. M.; Zhao, X.; Ding, Y; Bottomley, L. A. *J. Am. Chem. Soc.* **1995**, *117*, 12891.
(13) Ribou, A.-C.; Launay, J.-P.; Sachtleben, M. L.; Li, H.; Spangler, C. W. *Inorg. Chem.* **1996**, *35*, 3735.
(14) Patoux, C.; Coudret, C.; Launay, J.-P.; Joachim, C.; Gourdon, A. *Inorg. Chem.* **1997**, *36*, 5037.
(15) Robin, M. B.; Day, P. *Adv. Inorg. Chem. Radiochem.* **1967**, *10*, 247.
(16) Hush, N. S. *Prog. Inorg. Chem.* **1967**, *8*, 391.

10.1021/ic801801m CCC: $40.75
Published on Web 04/03/2009

requires an intimate familiarization with the variation of the electronic energy as a function of the nuclear coordinates.[17,18] For instance, Piepho, Krausz, and Schatz[19] and Ondrechen and co-workers[20] have developed models to analyze the MV dynamics in the Creutz−Taube ion.[21] Piepho's molecular orbital based method[22] has also been used. Regardless of the information one wishes to obtain in relation to a given MV compound's electronic interactions, potential energy surface (PES) diagrams provide the greatest insight into the delocalization-to-localization transition. The construction of these PESs with respect to different classes of MV compounds has been described in relation to the derivation of the nature of the IVCT band.

Recently, density functional theory (DFT) and time-dependent DFT (TDDFT) have been used to describe various properties of small to large transition-metal containing compounds with a high degree of success.[23] On the other hand, there has been a limited use of DFT in describing the electronic structure of MV compounds[24] predominantly because of the inherent difficulties associated with DFT and TDDFT methods such as the self-interaction error[25] and the inability to adequately model charge-transfer over larger distances.[26] In spite of these difficulties, attempts have been made at describing MV properties using a DFT approach with the Creutz−Taube ion[27] along with other MV compounds.[28,29] The majority of previous studies focused on the description of the ground-state PES during a particularly important vibration or set of vibrations in class III compounds and, very rarely, class II compounds.[30] Class III MV compounds have been successfully characterized by DFT techniques, but characterization of class II compounds so far has been a difficult task because of the misrepresentation of the correct localized ground state. The excited-state properties of transition-metal based class II MV compounds are even less well-known.

Recently, we have reported the MV state formation in polyferrocenyl containing porphyrins.[31−34] To accurately predict the MV behavior in these systems, one needs to find a reliable theoretical DFT-based approach which allows a correct description of mixed-valency in a relatively simple bisferrocenium system. As a first step, we explored a simple, well-known class II MV biferrocenium ($\mathbf{BF}^+$) cation, which was extensively characterized by temperature dependent Mössbauer,[35] UV−vis,[10] and resonance Raman[36] (rR) methods. As it shown below (and unlike in the case of some organic-based MV compounds[37]) it seems that the "standard" hybrid DFT methods are able to reproduce all energy- and spectroscopy-based benchmarks of the $\mathbf{BF}^+$ system.

Computational Methods

All DFT calculations were conducted using Gaussian 03.[38] The spin-unrestricted method has been used for all MV calculations without the counterion included. Molecular geometries were obtained using Becke's three-parameter hybrid exchange functional[39] and Lee−Yang−Parr nonlocal correlation functional[40]

(17) D'Alessandro, D. M.; Keene, F. R. *Chem. Soc. Rev.* **2006**, *35*, 424.
(18) (a) Brunschwig, B. S.; Sutin, N. *Coord. Chem. Rev.* **1999**, *187*, 233. (b) Brunschwig, B. S.; Creutz, C.; Sutin, N. *Chem. Soc. Rev.* **2002**, *31*, 168.
(19) (a) Piepho, S. B.; Krausz, E. R.; Schatz, P. N. *J. Am. Chem. Soc.* **1978**, *100*, 2996. (b) Wong, K. Y.; Schatz, P. N. *Prog. Inorg. Chem.* **1981**, *28*, 369.
(20) Zhang, L.-T.; Ko, J.; Ondrechen, M. J. *J. Am. Chem. Soc.* **1987**, *109*, 1666.
(21) Creutz, C.; Taube, H. *J. Am. Chem. Soc.* **1969**, *91*, 3988.
(22) Piepho, S. B. *J. Am. Chem. Soc.* **1988**, *110*, 6319.
(23) (a) Nemykin, V. N.; Hadt, R. G.; Belosludov, R. V.; Mizuseki, H.; Kawazoe, Y. *J. Phys. Chem. A* **2007**, *111*, 12901. (b) Nemykin, V. N.; Makarova, E. A.; Grosland, J. O.; Hadt, R. G.; Koposov, A. Y. *Inorg. Chem.* **2007**, *46*, 9591. (c) Nemykin, V. N.; Olsen, J. G.; Perera, E.; Basu, P. *Inorg. Chem.* **2006**, *45*, 3557. (d) Nemykin, V. N.; Basu, P. *Inorg. Chem.* **2003**, *42*, 4046. (e) Basu, P.; Nemykin, V. N.; Sengar, R. S. *Inorg. Chem.* **2003**, *42*, 7489. (f) Wang, F.; Ziegler, T. *J. Chem. Phys.* **2005**, *123*, 194102/1. (g) Seth, M.; Ziegler, T. *J. Chem. Phys.* **2005**, *123*, 144105/1. (h) Soldatova, A. V.; Kim, J.; Peng, X.; Rosa, A.; Ricciardi, G.; Kenney, M. E.; Rodgers, M. A. *J. Inorg Chem.* **2007**, *46*, 2080. (i) Ray, K.; George, S. D.; Solomon, E. I.; Wieghardt, K.; Neese, F. *Chem.−Eur. J.* **2007**, *13*, 2783. (j) Gorelsky, S. I.; da Silva, S. C.; Lever, A. B. P.; Franco, D. W *Inorg. Chim. Acta* **2000**, *300*, 698.
(24) (a) Barone, V.; Bencini, A.; Gatteschi, D.; Totti, F. *Chem.−Eur. J.* **2002**, *8*, 5019. (b) Wu, Q.; Van Voorhis, T. *J. Chem. Phys.* **2006**, *125*, 164105. (c) Wu, Q.; Van Voorhis, T. *J. Phys. Chem. A.* **2006**, *110*, 9212.
(25) Lundberg, M.; Siegbahn, P. E. M. *J. Chem. Phys.* **2005**, *122*, 224103.
(26) Hieringer, W.; Goeling, A. *Chem. Phys. Lett.* **2006**, *419*, 557.
(27) (a) Bencini, A.; Ciofini, I.; Daul, C. A.; Ferretti, A. *J. Am. Chem. Soc.* **1999**, *121*, 11418. (b) Chen, Z.; Bian, J.; Zhang, L.; Li, S. *J. Chem. Phys.* **1999**, *111* (24), 10926.
(28) Daul, C.; Fernandez-Ceballos, S.; Ciofini, I.; Rauzy, C.; Schläpfer, C.-W. *Chem.−Eur. J.* **2002**, *8*, 4392.
(29) Gorelsky, S. I.; Xie, X.; Chen, Y.; Fee, J. A.; Solomon, E. I. *J. Am. Chem. Soc.* **2006**, *128*, 16452.
(30) Bencini, A.; Gatteschi, D.; Mattesini, M.; Totti, F.; Cofini, I. *Mol. Cryst. Liq. Cryst.* **1999**, *335*, 665.
(31) Nemykin, V. N.; Barrett, C. D.; Hadt, R. G.; Subbotin, R. I.; Maximov, A. Y.; Polshin, E. V.; Koposov, A. Y. *Dalton Trans.* **2007**, *31*, 3378.
(32) Nemykin, V. N.; McGinn, M.; Koposov, A. Y.; Tretyakova, I. N.; Polshin, E. V.; Loim, N. M.; Abramova, N. V. *Ukr. Chem. J.* **2005**, *71*, 79.
(33) Nemykin, V. N.; Galloni, P.; Floris, B.; Barrett, C. D.; Hadt, R. G.; Subbotin, R. I.; Marrani, A. G.; Zanoni, R.; Loim, N. M. *Dalton Trans.* **2008**, 4233.
(34) Nemykin, V. N.; Kobayashi, N. *Chem. Commun.* **2001**, 165.
(35) (a) Mochida, T.; Takazawa, K.; Matsui, H.; Takahashi, M.; Takeda, M.; Sato, M.; Nishio, Y.; Kajita, K.; Mori, H. *Inorg. Chem.* **2005**, *44*, 8628. (b) Pannell, K. H.; Imshennik, V. I.; Maksimov, Yu. V.; Il'ina, M. N.; Sharma, H. K.; Papkov, V. S.; Suzdalev, I. P. *Chem. Mater.* **2005**, *17*, 1844. (c) Oda, T.; Nakashima, S.; Okuda, T. *Inorg. Chem.* **2003**, *42*, 5376. (d) Jiao, J.; Long, G. J.; Grandjean, F.; Beatty, A. M.; Fehlner, T. P. *J. Am. Chem. Soc.* **2003**, *125*, 7522. (e) Nakashima, S.; Ueki, Y.; Sakai, H.; Maeda, Y. *J. Chem. Soc., Dalton Trans.* **1996**, 139. (f) Kramer, J. A.; Herbstein, F. H.; Hendrickson, D. N. *J. Am. Chem. Soc.* **1980**, *102*, 2293.
(36) Williams, R. D.; Petrov, V. I.; Lu, H. P.; Hupp, J. T. *J. Phys. Chem. A.* **1997**, *101*, 8070.
(37) Blomgren, F.; Larsson, S.; Nelsen, S. F. *J. Comput. Chem.* **2001**, *22*, 655.
(38) Frisch, M. J.; Trucks, G. W.; Schlegel, H. B.; Scuseria, G. E.; Robb, M.; Cheeseman, J. R.; Montgomery, J. A.; Vreven, J. A.; Kudin, K. N.; Burant, J. C.; Millam, J. M.; Iyengar, S. S.; Tomasi, J.; Barone, V.; Mennucci, B.; Cossi, M.; Scalmani, G.; Rega, N.; Petersson, G. A.; Nakatsuji, H.; Hada, M.; Ehara, M.; Toyota, K. ; Fukuda, R.; Hasegawa, J.; Ishida, M.; Nakajima, T.; Honda, Y.; Kitao, O.; Nakai, H.; Klene, M.; Li, X.; Knox, J. E.; Hratchian, H. P.; Cross, J. B.; Adamo, C.; Jaramillo, J; Gomperts, R.; Stratmann, R. E.; Yazyev, O.; Austin, A. J.; Cammi, R.; Pomelli, C.; Ochterski, J. W.; Ayala, P. Y.; Morokuma, K.; Voth, G. A.; Salvador, P.; Dannenberg, J. J.; Zakrzewski, V. G.; Dapprich, S.; Daniels, A. D.; Strain, M. C.; Farkas, O.; Malick, D. K.; Rabuck, A. D.; Raghavachari, K.; Foresman, J. B.; Ortiz, J. V.; Cui, Q. ; Baboul, A. G. ; Clifford, S. ; Cioslowski, J.; Stefanov, B. B.; Liu, G.; Liashenko, A.; Piskorz, P.; Komaromi, I.; Martin, R. L.; Fox, D. J.; Keith, T.; Al-Laham, M. A.; Peng, C. Y.; Nanayakkara, A.; Challacombe, M.; Gill, P. M. W.; Johnson, B.; Chen, W.; Wong, M. W.; Gonzalez, C.; Pople, G. A. *Gaussian 03*, Revision C.02; Gaussian, Inc: Wallingford, CT, 2004.
(39) Becke, A. D. *Phys. Rev. A* **1988**, *38*, 3098–3100.
(40) Lee, C.; Yang, W.; Parr, R. G. *Phys. Rev. B* **1988**, *37*, 785–789.

(B3LYP) level coupled with Wachter's full-electron and 6-311G(d) basis sets for iron and all other atoms, respectively. In the case of the Hartree−Fock dependency studies, 13 standard exchange-correlation functionals (X_α, SVWN, HFS, BP86, BPW91, BLYP, VSXC, B3P86, B3PW91, B3LYP, B98, PBE1PBE, and BHandH-LYP) were used. In addition, various amounts of Hartree−Fock exchange were also incorporated into the B3LYP exchange correlation functional using the appropriate IOps commands available in Gaussian 03. In this case, the amount of Hartree−Fock exchange was varied between 5 and 30% in 5% increments (these are mentioned as B3LYP-xx functionals below). For all optimized structures, frequency calculations were carried out to determine whether optimized geometries represented either local minima, transition states, or higher order saddle points. At all stationary points found, additional stability calculations were conducted to ensure that the final wave function is stable. In the cases when wave function instability was found, the wave function was reoptimized using standard Gaussian 03 procedures. A variety of single point calculations have been conducted (i.e., energy, property, and TDDFT), and employed Wachter's full-electron basis set for the iron atom and a 6-311G(d)[41] basis set for carbon and hydrogen. In the case of the TDDFT calculations, hybrid B3LYP was used with the same basis sets as the single point calculations described above. Geometries of $\mathbf{BF}^+$ were also optimized in dichloromethane and acetonitrile. All solvent media geometry optimizations and TDDFT calculations were conducted using the polarized continuum model (PCM) approach[42] implemented into Gaussian 03 software.

Electron densities on the ^{57}Fe nuclei in the compounds of interest were calculated using AIM2000[43] program. Mössbauer quadrupole splittings (ΔE_Q) and asymmetry parameters (η) were calculated using DFT predicted principle components of the electric field gradient tensor (V_{ii}) at the ^{57}Fe nucleus as previously described.[44] The percentage of atomic orbital contributions to molecular orbitals was calculated using VMOdes program.[45]

Results and Discussion

1. Stationary Point Geometries and Energies. Within the simplest two-state model borders, the $\mathbf{BF}^+$ cation can be characterized by the MV class II energy profile presented in Figure 1.[46] To explore potential energy landscapes in the class II $\mathbf{BF}^+$ cation, it is necessary to gain insight into the structures of key stationary points of the lower and upper adiabatic PESs. These points include localized $Fe^{II}-Fe^{III}$ and $Fe^{III}-Fe^{II}$ global minima structures at $X \sim 0$ and $X \sim 1$ normal coordinates, respectively, as well the transition state located at $X = 0.5$ (Figure 1). Similarly, knowledge of localized and delocalized excited-state geometries located on the upper adiabatic PES can provide an additional insight on the electron transfer process. Geometrical distortions occuring during valence trapping in class II MV compounds can often be observed in X-ray diffraction studies. Although crystal structures of neutral biferrocene and MV $\mathbf{BF}^+$ have been reported in the literature,[47] these cannot be used directly in our computational study because of the following: (i) in the case of $\mathbf{BF}^+$, one or both unsubstituted cyclopentadienyl (Cp) rings show positional disorder between eclipsed and staggered conformations, which is a typical disorder for metallocene structures; (ii) the degree of spin localization/delocalization in MV biferrocenium ions is easily perturbed by crystal packing interactions between the binuclear cation and corresponding anion. For instance, in solution, $\mathbf{BF}^+$ complexes behave as localized class II compounds, while in the solid state, depending on the nature of a counterion, they can show a high degree of delocalization at elevated temperatures as shown by Mössbauer spectroscopy.[35] First, we explore the stationary points of $\mathbf{BF}^+$ using a hybrid B3LYP exchange-correlation functional. Overall, three stationary points (at $X \sim 0$, $X \sim 1$, and $X = 0.5$) on the lower and one stationary point on the upper adiabatic PESs were located, which are summarized in Table 1.

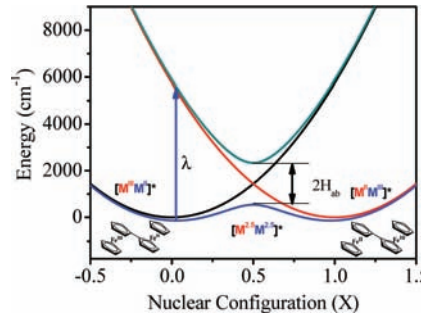

Figure 1. Two-state PES profile of $\mathbf{BF}^+$ constructed using experimentally determined[36] values of λ (5750 cm^{-1}) and H_{ab} (900 cm^{-1}).

1.1. Localized $Fe^{II}-Fe^{III}$ Global Minimum Structure of BF^+ (Lower Adiabatic PES with $X \sim 0$ and $X \sim 1$). It is commonly accepted that DFT methods tend to stabilize the valence delocalized states in experimentally proven class II compounds. Surprisingly, the hybrid B3LYP exchange-correlation functional has correctly predicted the valence-localization for the ground state of $\mathbf{BF}^+$. The DFT predicted global minimum has C_1 symmetry (labeled as $\mathbf{C_1m}$ below), with a slightly distorted ($\theta \sim 2.5$ and 4.5° for Fe^{II} and Fe^{III} units, respectively, Figure 2) eclipsed conformation on both ferrocene subunits (Supporting Information, Table 1). From Supporting Information, Table 1 and, specifically, the r_1, r_2, r_3, and r_4 average Cp−Fe optimized distances, it is clear that upon oxidation the neutral biferrocene system undergoes significant distortion (~0.05 Å), and this distortion occurs

(41) McLean McLean, A. D.; Chandler, G. S. *J. Chem. Phys.* **1980**, *72*, 5639–5948.
(42) Miertus, S.; Scrocco, E.; Tomasi, J. *J. Chem. Phys.* **1981**, *55*, 117.
(43) (a) Biegler-Konig, F. *AIM 2000*, version 1.0; University of Applied Science: Bielefeld, Germany. (b) Bader, R. F. W. *Atoms in Molecules A Quantum Theory*; Oxford University Press: Oxford, 1990.
(44) Nemykin, V. N.; Hadt, R. G. *Inorg. Chem.* **2006**, *45*, 8297.
(45) Nemykin, V. N.; Basu, P. *VMOdes: Virtual Molecular Orbital Description Program for Gaussian, GAMESS, and HyperChem, revision A 7.1*, 2005.
(46) Similar to Creutz−Taube ion, three IVCT bands are expected for $\mathbf{BF}^+$ (Table 4). In addition, two d-d transitions in the low-energy envelope of the UV-vis spectrum of $\mathbf{BF}^+$. Since the only one transition (first IVCT band) is the major contributor in this region of the spectrum, the two-state model still can be considered as an acceptable approximation for the description of mixed-valence behavior of $\mathbf{BF}^+$, similar to that described for dicopper and Creutz−Taube mixed-valence compounds.
(47) (a) Konno, M.; Hyodo, S.; Iijima, S. *Bull. Chem. Soc. Jpn.* **1982**, *55*, 2327. (b) Kramer, J. A.; Herbstein, F. H.; Hendrickson, D. N. *J. Am. Chem. Soc.* **1980**, *102*, 2293. (c) Cowan, D. O.; Shu, P.; Hedberg, E. L.; Rossi, M.; Kistenmacher, T. J. *J. Am. Chem. Soc.* **1979**, *101*, 1304.

Table 1. Energetics, Spin Densities, And Nature (i.e., Stationary Point, Transition State, etc.) of the B3LYP Optimized Geometries of the Initial Analysis of the Lower Adiabatic Surface

geom.	X	WF[g]	relative energy (cm^{-1})	ZPE (cm^{-1})	relative ZPE (cm^{-1})	imag. freqs, cm^{-1} (symmetry)	spin density Fe^{III}/Fe^{II}
				Gas-Phase			
C_1 (**C_1m**)	∼0	y	0	69990	0		1.28/0.02
C_1[a]	∼0	y	25	69980	10	22 A	1.28/0.01
C_1[b]	∼0	y	185	69950	140	28 A	1.28/0.01
C_2 (**C_2ts**)	0.5	y	538	69810	360	642 B	0.98/0.34
C_2	0.5	n	551	70470	1030		0.67/0.67
C_i	0.5	y	549	69800	360	643 A_u, 16 A_u	0.98/0.34
C_i	0.5	n	562	70450	1030		0.67/0.67
C_{2h}[c]	0.5	y	569	69730	310	636 B_g, 33 B_g, 15 B_g	0.99/0.33
C_{2h}[c]	0.5	n	584	70350	950	24 A_u, 21 B_g	0.67/0.67
C_{2h}[d]	0.5	y	751	69750	510	774 B_g, 31 B_g, 19 B_g	0.95/0.38
C_{2h}[d]	0.5	n	759	70410	1000	25 B_g	0.67/0.67
				PCM			
C_1[e]	∼0	y	0	69960	0		1.27/0.02
C_2[e]	0.5	y	672	69790	850	645 B	0.98/0.34
C_2[e]	0.5	n	1419	70440	940		0.70/0.70
C_1[f]	∼0	y	0	69960	0		1.27/0.02
C_2[f]	0.5	y	670	69780	850	640 B	0.98/0.34
C_2[f]	0.5	n	1559	70440	1080		0.67/0.67

[a] Fc conformation is D_{5h} and D_{5d}. [b] Fc conformation is both D_{5d}. [c] Fc conformation is both D_{5h}. [d] Fc conformation is both D_{5d}. [e] CH_2Cl_2. [f] CH_3CN. [g] Wave function stability.

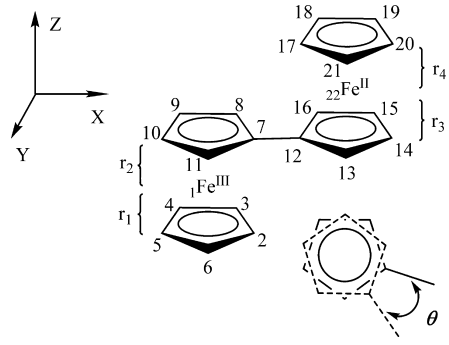

Figure 2. Labeling scheme and Cartesian axis in $\mathbf{BF}^+$. r_1 and r_2 are distances pertaining to ferric sites and r_3 and r_4 are ferrous.

on the ferric center, while the ferrous center remains unchanged and these distortions are in excellent agreement with X-ray diffraction studies on **BF** and $\mathbf{BF}^+$.[47] In addition, there are two other localized transition states within 25 and 185 cm^{-1} (10 and 143 cm^{-1}; ZPE corrected) of **C_1m** with one and two staggered "D_{5d}" ferrocene Cp ring conformations, respectively (Table 1). An analysis of the calculated imaginary frequencies of these transition states clearly indicate that the staggered "D_{5d}" conformation should be distorted toward smaller dihedral angles, θ, to achieve the global minimum conformation.

1.2. Delocalized "$Fe^{2.5}$-$Fe^{2.5}$" structure of $\mathbf{BF}^+$ (lower adiabatic PES with $X = 0.5$). For class II $\mathbf{BF}^+$ system, the transition state involved in adiabatic electron transfer should be symmetric[17,18] and indeed, three structures of $\mathbf{BF}^+$ of C_2, C_i, and C_{2h} symmetries with similar energies were found in the $X = 0.5$ region (Figure 1, Tables 1 and Supporting Information, Table 1). All symmetric structures have a large instability with respect to electron transfer, which can be characterized by their largest imaginary frequency. The lowest energy symmetric structure has C_2 symmetry (referred as **C_2ts**) and is the transition state of interest, while C_i symmetric structure is only 11 cm^{-1} (2 cm^{-1}; ZPE corrected) higher in energy than **C_2ts**. Two different C_{2h} structures were also located on the PES at the $X = 0.5$ region. One of these has two eclipsed "D_{5h}" conformations of the Cp-Fv ligands and the other has two staggered "D_{5d}" conformations of the Cp ligands with energies 31 and 213 cm^{-1} higher as compared to that found for the **C_2ts** structure, respectively.

1.3. Localized $\mathbf{Fe^{II}-Fe^{III}}$ Excited-State Structure of $\mathbf{BF}^+$. Following an Fe^{III} centered symmetric vibrational coordinate, ν_{11} (discussed below) in the **C_1m** structure, it is possible to optimize the geometry of the excited state of the localized $Fe^{II}-Fe^{III}$ $\mathbf{BF}^+$. This excited state (referred as **C_1ex**) can formally have been obtained as a result of an $Fe^{III}-Fe^{III}$ d-d transition in agreement with our TDDFT calculations discussed below. The ferrous site in **C_1ex** is essentially identical to that in the ground state. However, the ferric site has less ferric character than **C_1m**, and this can be seen from the differences in r_1 and r_2, which is ∼0.03 Å in both cases (∼0.05 Å in the ground state).

Overall, B3LYP exchange-correlation functional gives an accurate description of the $\mathbf{BF}^+$ ground state (**C_1m**, localized $Fe^{II}-Fe^{III}$ structure). The lowest energy symmetric transition state (**C_2ts**) is described by a C_2 symmetric structure that is 538 cm^{-1} (358 cm^{-1} with ZPE correction) higher in energy as compared to the **C_1m** geometry. The first excited state is located 6541 cm^{-1} above the **C_1m** geometry in perfect agreement with out TDDFT data described below. Predicted geometries and relative energies of **C_1m** and **C_2ts** structures in dichloromethane and acetonitrile using a PCM approach remain close to those calculated in the gas phase (Table 1). In both solvents, the **C_1m** structure remains the global minimum with an energy difference of 502 and 515 cm^{-1} from **C_2ts** found for dichloromethane and acetonitrile, respectively.

2. Electronic Structure. In a simplified picture, the electronic structure of a class II MV compound with two

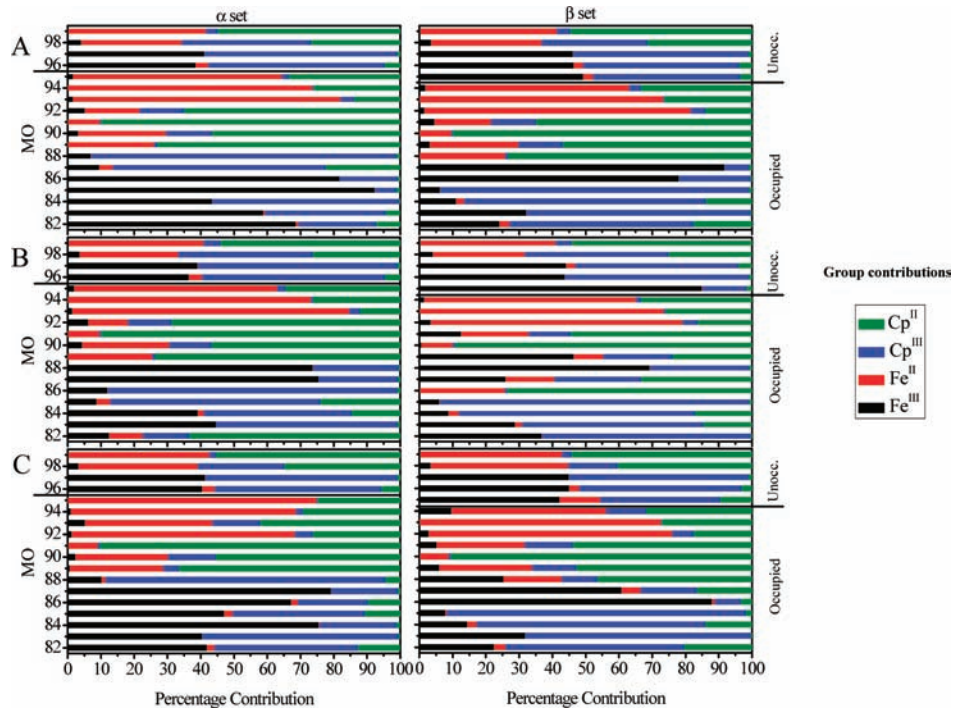

Figure 3. α and *β* MO composition for (A) **C$_1$m**; (B) **C$_1$ex**; and (C) **C$_1$ts** using the B3LYP exchange-correlation functional. Lines indicate the HOMO−LUMO gap.

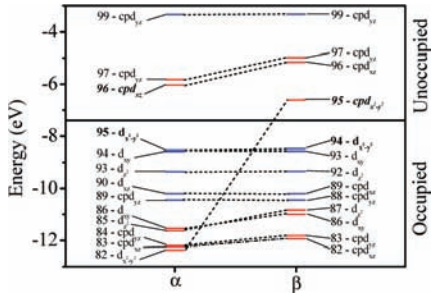

Figure 4. Fe^{II} (blue) and Fe^{III} (red) d manifold electronic structure of **C$_1$m** geometry.

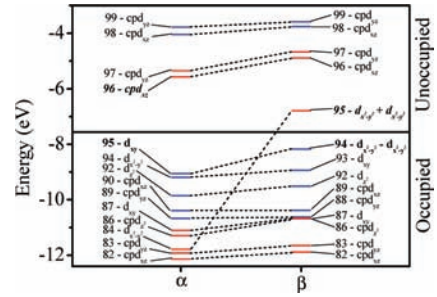

Figure 5. Fe^{II} (blue) and Fe^{III} (red) d manifold electronic structure of the **C$_2$ts**.

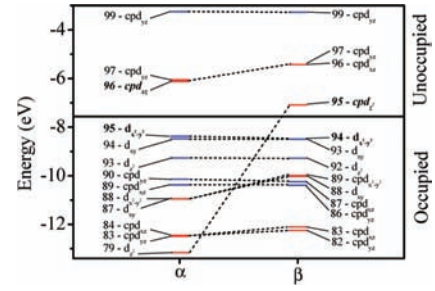

Figure 6. Fe^{II} (blue) and Fe^{III} (red) d manifold electronic structure of the **C$_1$ex** geometry.

interacting metal centers of different oxidation states will show distinct M^{n+} and $M^{(n+1)+}$ character with a ***localized*** singly occupied molecular orbital (SOMO) on the respective metal center. In the case of class III compounds, however, indistinguishable $M^{(n+1/2)+}$ and $M^{(n+1/2)+}$ sites are found, with a SOMO that is completely ***delocalized*** over both metal centers. Thus, in the case of the class II **BF$^+$**, electron transfer occurs between two localized Fe^{II} and Fe^{III} orbitals, while within the borders of class III complexes, the electron transfer occurs between two orbitals delocalized over both metallo-centers. Supporting Information, Figure 1 displays the *β* HOMO and LUMO obtained using a B3LYP exchange-correlation functional for all stationary points discussed above. The percentage contributions to the important MOs for **C$_1$m**, **C$_2$ts**, and **C$_1$ex** are listed in Supporting Information, Tables 2−4, respectively, as well as graphically shown in Figures 3−6.

2.1. *C*$_1$ Localized Global Minimum of BF$^+$ (C$_1$m). The MO diagram of **C$_1$m** is presented in Figure 4. The localized nature of the electronic structure of **C$_1$m** is evident from the analysis of its MOs (Figure 3 and Supporting Information, Figure 2). The HOMO through HOMO-2 are predominantly Fe^{II} based MOs with x^2-y^2, xy, and z^2 character, respectively. The Fe^{III}-centered HOMO-5 and HOMO-6 MOs are significantly more stable as compared to Fe^{II} based MOs. MOs 96 and 97 are predominantly Cp-ligand-based π^* orbitals with almost equal contribution from Fe^{III} d_{xz} and d_{yz} orbitals. The SOMO is a predominantly Fe^{III}-based $d_{x^2-y^2}$ orbital, which creates the opportunity for three IVCT transitions originating from the Fe^{II}-based HOMO through HOMO-2. The *β* LUMO

is energetically well separated from other unoccupied orbitals and interacts in a bonding fashion with a bridging π^* orbital ($C_{ipso}-C_{ipso}$), forming the molecular orbital pathway for intramolecular electron transfer.

2.2. C_2 Transition State of BF^+ (C_2ts). The MO diagram of **C_2ts** is presented in Figure 5, while the molecular orbital compositions are listed in Supporting Information, Table 3 and shown in Figure 3 and Supporting Information, Figure 3. In general, the adiabatic electron transfer transition state is a symmetric structure, in which α and β sets contain d orbitals that are linear combinations of one another and a delocalized electronic structure is obtained by default. This delocalized wave function, however, is unstable, and once the wave function is optimized, the electronic structure shows localized character. This can be expected because of the smaller rate of electron transfer in the case of the symmetric class II transition state as compared to a class III delocalized structure that can be represented by a single welled potential.[17,19] It is also in perfect agreement with the transition state description according to which the transition state for class II MV compounds must have a symmetric geometry but have asymmetric electron localization over two transition metal ions.[19] The HOMO through HOMO-2 of **C_2ts** are predominantly Fe^{II} based x^2-y^2, xy, and z^2 MOs, respectively. The β-set HOMO of **C_2ts** is ∼47% and ∼10% of Fe^{II} and Fe^{III} based, respectively. LUMO of **C_2ts** has ∼42% and ∼12% Fe^{III} and Fe^{II} character, respectively. HOMO and LUMO in **C_2ts** represent out of phase and in phase combinations of x^2-y^2 orbitals, respectively. The Fe d orbitals interact in a bonding fashion with both π (in the case of the HOMO) and π^* (in the case of the LUMO) orbitals of the $C_{ipso}-C_{ipso}$ bridge (Supporting Information, Figure 1). These interactions form the exchange pathway ($x^2-y^2-\pi^*-x^2-y^2$) for electron transfer in **C_2ts**, which can serve as the primary electron transfer pathway for thermally activated electron transfer between **C_1m** structures located at $X \sim 0$ and $X \sim 1$ (Figure 1).

2.3. C_1 Localized Excited State of BF^+ (C_1ex). The localized excited state, **C_1ex**, is coupled to ν_{11} (Supporting Information, Figure 6), a symmetric stretch localized on the Fe^{III} center. Analysis of the electronic structure of the fully optimized geometry along with TDDFT data on **C_1m** indicated that the excited state originates from an Fe^{III} $d_{x^2-y^2} \rightarrow d_{z^2}$ d-d transition, which is the third TDDFT predicted excited state (Supporting Information, Table 3). While TDDFT predicts a vertical excitation energy of 7091 cm^{-1} for this d-d transition, the fully optimized excited-state structure is 6541 cm^{-1} higher in energy than **C_1m** and is represented by a single electron excitation from a β $Fe^{III}z^2$ (87β) orbital to the β LUMO ($CpFe^{III}x^2-y^2$ (95β)) bonding MO. The MO diagram for **C_1ex** is displayed in Figure 6, and the orbital composition for selected MOs is provided in Figure 3 and Supporting Information, Table 4. The electronic structure of **C_1ex** is essentially identical to that of **C_1m** except for the fact that, as expected from the nature of the electronic transition, the $Fe^{III}z^2$ and the LUMO of the ground state have switched in **C_1ex**.

3. Spectroscopic Characteristics of Stationary PES Points. 3.1. Mössbauer Spectroscopy. Temperature dependent Mössbauer studies on MV biferrocenium systems provided a unique opportunity to study the influence of crystal packing forces and types of counterions on the thermal dependency of the intramolecular electron transfer process.[35] In the majority of complexes, class II behavior dominates, resulting in the observation of individual ferrocene- and ferricinium-type Mössbauer doublets (Supporting Information, Table 5).[10] In several cases, however, the barrier to thermal electron transfer was lowered as a result of cation−anion interactions and/or packing forces and as a result the high-temperature Mössbauer spectrum consists of a single "average-valence" doublet suggesting a fast (∼10^{-7} s) electron transfer rate between Fe^{II} and Fe^{III} centers.[48] Thus, it should be expected that the Mössbauer spectra parameters of the **C_1m** will resemble low-temperature Mössbauer spectra of the **BF^+** cation, while those calculated for the **C_2ts** will be close to Mössbauer spectra of the "average-valence" doublet.

DFT calculations of Mössbauer spectra parameters in ferrrocenes have been reported,[44] but similar calculations on biferrocene and MV **BF^+** are not available in the literature. The use of "pure" DFT exchange-correlation functionals for the calculation of Mössbauer parameters in ferrocenes was advocated because of the very poor performance of any "hybrid" DFT based approaches.[44] This requirement leads to a problem in the case of MV **BF^+**. First, the self-interaction error in pure DFT methods stabilizes delocalized states,[25] and results in artificial delocalization of the unpaired electron, compromising the calculation of Mössbauer spectra parameters. When hybrid exchange-correlation functionals are used, the spin delocalization problem can be averted but in this case, the calculated Mössbauer spectra parameters of ferrocenes become inaccurate.[44] To overcome the problem with spin delocalization one should artificially localize the unpaired electron on the Fe^{III} center. This can be accomplished by applying a field in the appropriate direction (chosen to be along the Fe−Fe bond, x-axis, in **BF^+**, Figure 2). Supporting Information, Table 5 lists calculated Mössbauer parameters for **BF** along with the **BF^+** with and without an applied field. The quadrupole splitting of the neutral biferrocene is slightly overestimated (2.533 mm/s) while the isomer shift is slightly underestimated (0.419 mm/s), although in reasonable agreement with experiment and previous calculations on ferrocene-containing systems.[44,49] In **BF^+**, with no field applied, the calculated (BPW91) spin densities are 0.46 and 0.76, while quadrupole splittings are 1.622 and 1.281 mm/s for Fe^{II} and Fe^{III}, respectively, clearly suggesting electron delocalization in **BF^+** because of the wrong description of spin density. However, once a small field is applied (0.0020 au), the spin densities on Fe^{II} and Fe^{III} begin to shift toward the correct description, while the

(48) Gütlich, P. , Ensling, J. In *Inorganic Electronic Structure and Spectroscopy*; Lever, A. B. P., Solomon, E. I., Eds.; John Wiley & Sons: New York, 1999; Vol. *I*, pp 161−212.
(49) Herber, R. H.; Nowik, I.; Grosland, J. O.; Hadt, R. G.; Nemykin, V. N. *J. Organomet. Chem.* **2008**, *693*, 1850.

Table 2. TDDFT (B3LYP) Predicted Vertical Excitation Energies for the $\mathbf{C_1m}$ Geometry

trans.	λ, cm^{-1}	f	assignment	transitions and expansion coefficients
1	3410	0	$Fe^{III}xy \rightarrow cpFe^{III}x^2-y^2$	$86\beta \rightarrow 95\beta$ (1.39); $86\beta \rightarrow 105\beta$ (−0.27)
2	6490	0.0046	$Fe^{II}x^2-y^2 \rightarrow cpFe^{III}x^2-y^2$ (IVCT)	$95\alpha \rightarrow 96\alpha$ (−0.49); $95\alpha \rightarrow 98\alpha$ (0.40); $94\beta \rightarrow 95\beta$ (0.87); $94\beta \rightarrow 96\beta$ (0.25); $94\beta \rightarrow 98\beta$ (−0.43)
3	7090	0.0003	$Fe^{III}z^2 \rightarrow cpFe^{III}x^2-y^2$	$87\beta \rightarrow 95\beta$ (0.96)
4	7620	0	$Fe^{II}xy \rightarrow cpFe^{III}x^2-y^2$ (IVCT)	$94\alpha \rightarrow 96\alpha$ (−0.32); $94\alpha \rightarrow 98\alpha$ (0.43); $93\beta \rightarrow 95\beta$ (0.79); $93\beta \rightarrow 98\beta$ (−0.53)
5	11100	0.0001	$Fe^{II}xy \rightarrow cpFe^{III}x^2-y^2$ (IVCT)	$94\alpha \rightarrow 96\alpha$ (0.57); $94\alpha \rightarrow 98\alpha$ (−0.49); $95\alpha \rightarrow 96\alpha$ (−0.30); $93\beta \rightarrow 95\beta$ (0.56)
6	11560	0.0193	$Fe^{II}xy \rightarrow cpFe^{II}yz$ $Fe^{II}x^2-y^2 \rightarrow cpFe^{III}x^2-y^2$	$94\alpha \rightarrow 99\alpha$ (0.51); $95\alpha \rightarrow 96\alpha$ (0.41); $95\alpha \rightarrow 98\alpha$ (−0.44); $93\beta \rightarrow 99\beta$ (−0.40); $94\beta \rightarrow 95\beta$ (0.48); $94\beta \rightarrow 98\beta$ (0.31)
7	12360	0.0076	$Fe^{II}xy \rightarrow cpFe^{II}yz$	$94\alpha \rightarrow 99\alpha$ (−0.57); $95\alpha \rightarrow 96\alpha$ (0.37); $93\beta \rightarrow 99\beta$ (0.67)
8	12790	0	$Fe^{II}x^2-y^2 \rightarrow cpFe^{II}yz$	$94\alpha \rightarrow 96\alpha$ (0.26); $95\alpha \rightarrow 99\alpha$ (0.74); $94\beta \rightarrow 99\beta$ (−0.81)
9	13870	0.0043	$Fe^{II}z^2 \rightarrow cpFe^{III}x^2-y^2$	$93\alpha \rightarrow 96\alpha$ (−0.27); $93\alpha \rightarrow 98\alpha$ (0.31); $94\alpha \rightarrow 99\alpha$ (−0.32); $92\beta \rightarrow 95\beta$ (0.68); $92\beta \rightarrow 98\beta$ (−0.41); $93\beta \rightarrow 99\beta$ (0.31)
10	14890	0.003	$Fe^{II}x^2-y^2 \rightarrow cpFe^{II}xz$	$95\alpha \rightarrow 96\alpha$ (0.56); $91\beta \rightarrow 95\beta$ (0.35)

calculated quadrupole splittings undergo a shift toward distinct ferrocene- and ferricinium-type sites. At approximately 0.0055 au the calculated quadrupole splittings and isomer shifts get close to experimental values while the calculated spin densities resemble an expected charge localized system.

The calculation of the Mössbauer spectra parameters for a system with a fast thermal electron transfer rate can be achieved using $\mathbf{C_2ts}$. Again, good agreement between theory and experiment was observed suggesting that our optimized $\mathbf{C_1m}$ and $\mathbf{C_2ts}$ indeed resemble the low-temperature ground- and high-temperature transition state geometries of the $\mathbf{BF}^+$ (Supporting Information, Table 5).

3.2. UV−vis Spectroscopy and TDDFT Calculations. The formation of the IVCT band(s) in the near-IR region of the absorption spectrum is a clear indication of the formation of MV states.[16,17] The characteristics of this band have been employed in the evaluation of the extent of electronic communication (H_{ab}) between metals of different oxidation states using the well-known Hush formalism.[16] When the position and the intensity (i.e., oscillator strength) of the IVCT band can be accurately predicted computationally, the value of H_{ab} can be easily estimated from these calculations. In the recent years, TDDFT has offered a reliable method for the calculation of the UV−vis spectra of open-shell systems including those of inorganic and organometallic complexes.[23] TDDFT, sometimes, however, has difficulties in systems where charge is being transferred over long distances,[26] and this is the case for the MV $\mathbf{BF}^+$ because the Fe^{II} and Fe^{III} centers are separated by ∼5 Å. On the other hand, Gorelsky and Solomon have recently shown that TDDFT can be used for the accurate determination of the upper adiabatic PES profile in MV Cu_2S_2 clusters.[29] To test the reliability of the TDDFT approach for the accurate prediction of the vertical excitation energies in the MV $\mathbf{BF}^+$, we examined its first 10 vertical excitations, using the $\mathbf{C_1m}$ geometry and a B3LYP exchange-correlation functional (Table 2). In general, four transitions were predicted in the near-IR, IVCT band energy region. The first and the third transitions are pure $Fe^{III}(d_{xy}) \rightarrow Fe^{III}(d_{x^2-y^2})$ and $Fe^{III}(d_{z^2}) \rightarrow Fe^{III}(d_{x^2-y^2})$ d-d transitions. Transitions two and four, on the other hand, can be clearly attributed to IVCT bands, which originate from $Fe^{II}(d_{x^2-y^2}) \rightarrow Fe^{III}(d_{x^2-y^2})$ and $Fe^{II}(d_{xy}) \rightarrow Fe^{III}(d_{x^2-y^2})$ excitations. All four of these calculated transitions fall within the experimentally observed asymmetric IVCT band region although only the second transition (first IVCT band) is expected to be dominant based on its oscillator strength. It is interesting to note that the estimated energy of adiabatic transition (2480 cm^{-1}) calculated using commonly accepted method[50] is ∼1000 cm^{-1} lower in energy as compared to the first TDDFT predicted d-d transition (3410 cm^{-1}), which allows to estimate the magnitude of the reorganization energy in $\mathbf{BF}^+$.

4. Potential Energy Surfaces. The influence of the vibronic coupling mechanism on intramolecular electron transfer is very important for understanding MV compounds. In particular, the PKS[19] model has been extensively used in the study of the Creutz−Taube ion[24] and $\mathbf{BF}^+$.[51] A resonance Raman (rR) study[36] with laser excitation into the higher energy limit of the IVCT band of $\mathbf{BF}^+$ has enhanced three vibrations during the electron transfer process: (i) symmetric Cp−Fe−Fv stretch (280 cm^{-1}, the most strongly enhanced), (ii) Cp−Fe−Fv bending motion (504 cm^{-1}), and (iii) symmetric Cp breathing mode (1100 cm^{-1}). Each of these vibrations should have two counterparts, an Fe^{II} and Fe^{III} centered vibration, but the experimental resolution allowed only one peak for both Fe^{II} and Fe^{III} centered vibrations. Frequency analysis of $\mathbf{C_1m}$ revealed two separate symmetric stretch vibrations (Supporting Information, Figure 6), ν_{11} (∼280 cm^{-1}) and ν_{12} (∼287 cm^{-1}), centered on Fe^{III} and Fe^{II} sites, respectively, in excellent agreement with the rR experiment.[36] Since these vibrations are localized on individual iron centers, the PES scans should not lead to the electron transfer from the Fe^{II} to the Fe^{III} ion (Supporting Information, Figure 7). Indeed, *rigid* PES profiles of ν_{11} and ν_{12} vibrations are both quadratic and very similar to each other. It can be speculated, however, that if ν_{11} and ν_{12} are indeed the only vibrations responsible for the electron transfer in $\mathbf{BF}^+$, then such electron transfer can be achieved following PES scans on normalized symmetric and antisymmetric linear combinations of ν_{11} and ν_{12} (referred as Q_{symm} and Q_{anti}, respectively, Supporting Information, Figure 7), but again, no electron

(50) Nelsen, S. F.; Blackstock, S. C.; Kim, Y. *J. Am. Chem. Soc.* **1987**, *109*, 677.

(51) Boukheddaden, K.; Linares, J.; Varret, F. *Phys Rev. B.* **1993**, *47*, 14070. (b) Boukheddaden, K.; Linares, J.; Varret, F. *Phys Rev. B.* **1994**, *49*, 15659.

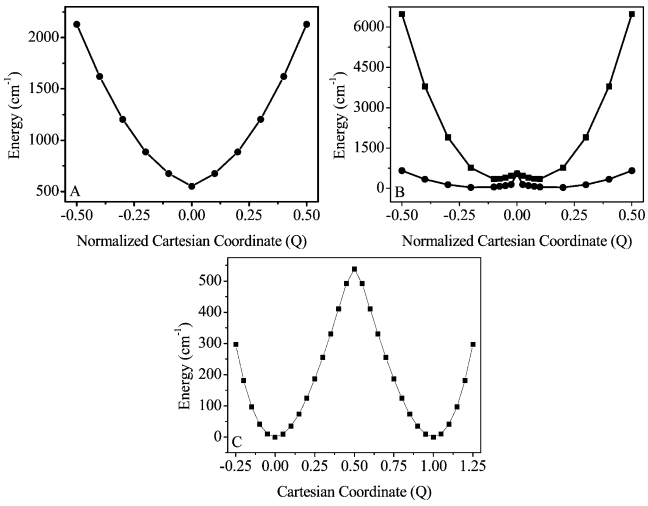

Figure 7. Important DFT (B3LYP) predicted PESs for the $\mathbf{C_2ts}$ geometry: (A) Q_{symm}; (B) *rigid* scan (squares) and *relax* scan (circles) of Q_i; (C) manually created Q_-.

transfer was observed for Q_{symm} and Q_{anti} profiles. It is clear that, by following all four discussed vibronic modes, the electron is trapped, and thus a combination of a larger number of vibronic modes must be considered to achieve electron transfer from the Fe^{II} to the Fe^{III} center.

Vibrational profiles for $\mathbf{C_2ts}$ can also yield valuable information relating to the electron transfer process in $\mathbf{BF}^+$. More specifically, starting from the symmetric $\mathbf{C_2ts}$, if the nuclear coordinates are varied in an antisymmetric fashion, a PES profile corresponding to this geometrical variation can be created and will be described as either a single- or double-welled potential. The temperature dependent MB studies do indicate that the MV biferrocene is a class II system with a thermal energy barrier to adiabatic electron transfer around $\sim$200 cm^{-1}, although the temperature at which the thermal barrier is overcome varies, depending on the counterion in the solid state and crystal-packing forces.[8−11] Frequency analysis of $\mathbf{C_2ts}$ reveals a large instability with respect to the antisymmetric stretch, which is represented by a large imaginary frequency (i642 cm^{-1}). In total, we investigate three vibrations of $\mathbf{C_2ts}$ (Supporting Information, Figure 6): (i) the symmetric stretch, Q_{symm}; (ii) the imaginary frequency, Q_i; and (iii) a manually created vibrational coordinate, Q_-. The calculated profile for Q_{symm} of $\mathbf{C_2ts}$ is very similar to that found in $\mathbf{C_1m}$ (Figure 7) except that the overall symmetric stretch, ν_{12} ($\sim$286 cm^{-1}), does not have separate Fe^{II} and Fe^{III} based components with close energies. The DFT predicted Q_i vibronic mode is asymmetric in nature and thus could be responsible for the electron transfer occurring upon going from $\mathbf{C_2ts}$ to the localized $\mathbf{C_1m}$. Indeed, several interesting observations on the PESs for *rigid* and *relaxed* scans of Q_i (Figure 7) should be discussed. First, although the *rigid* scan surface does show an energetic instability in Q_i, it does not lower the energy of the $\mathbf{C_2ts}$ to that of the $\mathbf{C_1m}$. Although the minimum on this surface occurs at 0.10 along the NCD, the energy of this minimum is significantly higher (ΔE = 349 cm^{-1}) than that of $\mathbf{C_1m}$. On the other hand, the *relaxed* scan surface does approach more closely the energy of $\mathbf{C_1m}$ (ΔE = 36 cm^{-1}), and the minimum on

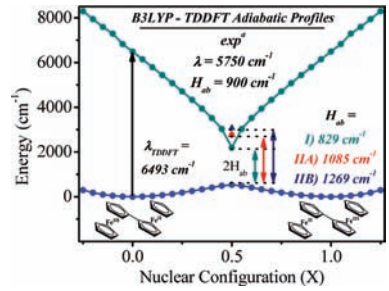

Figure 8. DFT and TDDFT predicted lower and upper adiabatic PESs for the $\mathbf{BF}^+$ cation.

this surface appears farther along the NCD, at 0.20. The results of the PES scans on Q_i suggest that although this vibration is very important in the electron transfer process in $\mathbf{BF}^+$, the other vibration, Q_-, should also be taken into consideration for the completion of electron transfer. For later consideration, we manually construct the crucial vibrational coordinate from the coordinates of both $\mathbf{C_1m}$ and $\mathbf{C_2ts}$ to be $X = 0$ and $X = 1$ in an effort to more clearly define the energetics and identity of the actual Q_- in which the atomic Cartesian coordinates of $\mathbf{C_1m}$, and that of $\mathbf{C_2ts}$ to be X = 0.5 (Figure 7C). Traversing this new coordinate brings us from $\mathbf{C_1m(1)}$ ($X \sim 0$) to $\mathbf{C_2ts}$ ($X = 0.5$) and back to $\mathbf{C_1m(2)}$ ($X \sim 1$, Figure 7C). Following the PES scan of Q_-, the electron can be transferred from the Fe^{II} to Fe^{III} center while negotiating the reaction coordinate from $X \sim 0$ to $X \sim 1$. Following this reaction coordinate, the single point energies of MV $\mathbf{BF}^+$ can be calculated. These calculations describe the actual vibronic process contributing to the electron transfer.

Overall, the partial vibronic analyses indicated the following: (i) electron transfer cannot be achieved using only Cp−Fe−Fv stretches of the $\mathbf{C_1m}$; (ii) although the asymmetric imaginary frequency Q_i observed for the $\mathbf{C_2ts}$ can be identified as the vibronic mode predominantly responsible for the electron transfer process in $\mathbf{BF}^+$, an accurate description of the electron transfer requires following a more complete Q_- vibronic mode. This mode represents the normal vibronic coordinate and describes the thermal electron transfer in $\mathbf{BF}^+$.

5. Full PES Profiles from Ground and Excited State Calculations. Having the single-point energies calculated along the Q_- vibronic coordinate, we can use TDDFT to estimate the nature of the upper adiabatic profile following the procedure recently suggested by Gorelsky and Solomon.[29] The resulting upper and lower adiabatic surfaces calculated using this approach are shown in Figure 8. The lower adiabatic surface is the Q_- representing intramolecular electron transfer as predicted from DFT because it directly connects $\mathbf{C_1m}$ and $\mathbf{C_2ts}$. The upper adiabatic surface is based on TDDFT predicted IVCT values. The *relaxed* PES scan for the Q_i vibronic coordinate is close to that calculated for the Q_- vibronic profile, while the corresponding *rigid* Q_i scan is less adequate in the description of the electron transfer process in $\mathbf{BF}^+$. Accordingly, it can be expected that TDDFT generated upper adiabatic profiles for *relaxed* and *rigid* scans will be significantly different with the former one close to

the PES scan of the Q– vibronic mode (Supporting Information, Figure 8). It can be seen that the ground-state surface governs the shape and curvature of the calculated excited-state profiles. The force constant of the *rigid* scan is large, and the change in energy with the change in NCD is large. On the other hand, the ground and excited-state adiabatic surfaces of the *relaxed* scan are relatively flat as compared to the *rigid* scan. The calculated λ for the *relaxed* surface is 6492 cm^{-1}, indicating that the *relaxed* minimum geometry is energetically similar to $\mathbf{C_1m}$ (36 cm^{-1} higher in energy). On the other hand, λ calculated for the *rigid* surface is only 4606 cm^{-1}, which is not surprising as the minimum geometry for the *rigid* scan PES is 349 cm^{-1} higher in energy than that of $\mathbf{C_1m}$.

6. Evaluation of H_{ab} in Mixed-Valence BF^+ Complex. Experimentally, within the borders of the Hush model formalism, H_{ab} can be evaluated on the basis of the shape of the IVCT band using the following equation: [16]

$$H_{ab} = [2.06 \times 10^{-2}(\nu_{max}\varepsilon_{max}\Delta\nu_{1/2})^{1/2}]/r_{ab} \quad (1)$$

where ν_{max}, ε_{max}, $\Delta\nu_{1/2}$, and r_{ab} are the energy at the band maximum, the extinction coefficient at the band maximum, the bandwidth at half-maximum, and the distance between the metal centers, respectively. Alternatively, H_{ab} can be calculated following the methods of Brunschwig, Creutz, and Sutin with the following equation:[18,19]

$$H_{ab} = [|\mu_{12}|\nu_{max}]/(er_{ab}) \quad (2)$$

where μ_{12} is the transition moment, e the electron charge.

Finally, H_{ab} can be calculated from the knowledge of lower and upper adiabatic PES surfaces, as well as the calculated energies of the stationary points and IVCT band. Brunschwig et al. develop and describe in detail the construction of PESs and the extraction of coupling elements H_{ab}.[17−19] Supporting Information, Figure 9 gives two such PES profiles describing a class III and a class II MV compounds. $\mathbf{BF^+}$ is a symmetric class II system, and, from the symmetric adiabatic surface (Figure 1), H_{ab} can be calculated in two different ways. First, from the splitting at the intersection ($X = 0.5$), H_{ab} can be calculated simply using (Method I):

$$H_{ab} = \Delta E/2 \quad (3)$$

where ΔE is the energy difference between the upper and lower adiabatic surfaces. This method involves a TDDFT calculation on the symmetric transition state $\mathbf{C_2ts}$. Second, when the energy of the transition state relative to that of the global minimum (E_{TS}) is known, H_{ab} can be calculated from the following equation (Method II):

$$H_{ab} = (\lambda/4) - E_{TS} \quad (4)$$

where λ is the reorganization energy. Because $\mathbf{BF^+}$ is a symmetrical system, λ is also the vertical excitation energy of the IVCT band and can be directly calculated using TDDFT methods. Energies of the $\mathbf{C_1m}$ and $\mathbf{C_2ts}$ state with and without zero-point energy correction can be obtained using DFT and can be used in the calculation of the H_{ab} matrix element. Methods IIA and IIB refer to when ZPE corrections are and are not employed to calculate E_{TS}, respectively. It can be expected that when using a DFT approach, the second method should be slightly more accurate because method I involves TDDFT calculations on the transition-state geometry stationary point.

The values of H_{ab} for $\mathbf{BF^+}$ obtained by the DFT based methods I, IIA, and IIB were calculated to be 829, 1085, and 1265 cm^{-1}, respectively, with the first one close to the experimental value of H_{ab} (900 cm^{-1}).[36] Since all of the above mentioned calculations were conducted in the gas phase, it is important to evaluate the H_{ab} value in $\mathbf{BF^+}$ in solution. In general, the reorganization energy of the class II $\mathbf{BF^+}$ complex in solution is simply equal to the energy of the IVCT band.[17−19] Accordingly, H_{ab} in solution for $\mathbf{BF^+}$ can be evaluated in exactly the same way as was already discussed for the gas-phase calculations, and these are listed in Supporting Information, Table 6 and again are in reasonable agreement with the experimental data. Overall, the B3LYP exchange-correlation functional indeed correctly predicts class II behavior of $\mathbf{BF^+}$ both in gas-phase and in solution with evaluated H_{ab} values close to those observed experimentally.

7. Hartree−Fock Dependency on the Mixed-Valence Character of the BF^+ Complex. 7.1. Electron Localization Versus Delocalization in the Class II BF^+ Complex as a Function of Exchange-Correlation Functional. Although the hybrid B3LYP exchange-correlation functional gives a reasonable estimation for the H_{ab} coupling parameter, the influence of the exchange-correlation functional on the degree of electron localization/delocalization in $\mathbf{BF^+}$ has never been discussed. To investigate such an influence, we have conducted several geometry optimizations of $\mathbf{BF^+}$ using LDA (LSDA, 0% of Hartree−Fock exchange), GGA (BP86 and BPW91, 0% of Hartree−Fock exchange), and hybrid (B3LYP-5-B3LYP-30, B98, ~22% of Hartree−Fock exchange, and PBE1PBE, 25% Hartree−Fock exchange) exchange-correlation functionals.

The results of the geometry optimizations are listed in Supporting Information, Table 7. The C_2 delocalized state is stabilized relative to the localized state for all LDA and GGA methods, as well as 5, 10, and 15% Hartree−Fock exchange B3LYP-xx exchange-correlation functionals. Any attempts to obtain the localized structure with these values of Hartree−Fock exchange failed. The completely delocalized wave functions of all of these methods are stable. However, when B3LYP is used (20% Hartree−Fock exchange) the localized state becomes the ground state, and the symmetric C_2 geometry becomes the adiabatic electron transfer transition state. When using B3LYP-25, B3LYP-30, B98, and PBE1PBE methods, a monotonic increase in the stabilization and destabilization of the localized and delocalized states, respectively, was found. The nature of the C_2 symmetric transition state predicted by various DFT methods is also interesting. In particular, the transition state predicted by B3LYP-20 is one that exhibits a large instability, and this large imaginary frequency (i642 cm^{-1}) represents instability with respect to intramolecular electron transfer.

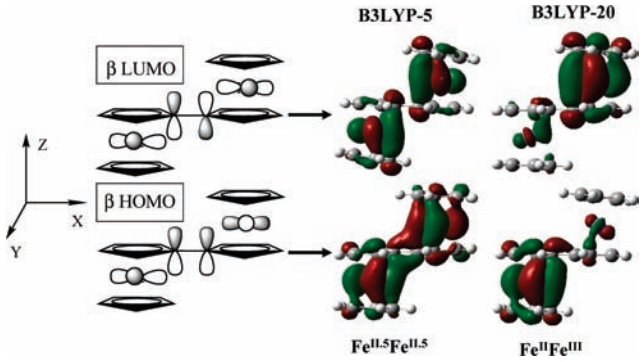

Figure 9. Major orbitals involved in the formation of the electron transfer pathway for class III (B3LYP-5) versus class II (B3LYP-20).

However, the transition states predicted by B3LYP-25, B3LYP-30, and PBE1PBE (~25% Hartree−Fock exchange) have only a small instability represented by a Cp ring twisting mode (Supporting Information, Table 7). It appears that the localized states are stable even in symmetric structures using the above 20% Hartree−Fock methods. B98, interestingly, gives a stable C_2 symmetric localized structure. Thus, in agreement to what has been already mentioned in the literature discussion, an inclusion of 20−30% of Hartree−Fock exchange looks to be a necessary requirement for the accurate description of a class $\mathbf{BF}^+$ system.

7.2. Ground State Identity and Degree of Spin Delocalization for the C_1 Symmetry Structure of BF^+ Cation as a Function of Exchange-Correlation Functional. Intuitively, it is expected that the amount of Hartree−Fock exchange involved in the exchange-correlation functional will directly influence the predicted stable ground-state wave function and ground-state geometry and thus the extent of delocalization or localization of $\mathbf{BF}^+$. Figure 9 shows β HOMO and LUMO plots resulting from two separate geometry optimizations, B3LYP-5 and B3LYP-20. Immediately, the effects of Hartree−Fock exchange on the degree of spin-localization are evident from the ground-state wave function represented by the β HOMO and LUMO. The, systematic investigation of the electronic structure of $\mathbf{BF}^+$ (at $\mathbf{C_1m}$ geometry) using the B3LYP optimized geometry and 14 different exchange-correlation functionals is presented in Supporting Information, Table 8. Supporting Information Figure 9A depicts the linear dependence ($r = 0.987$) of the β HOMO−LUMO gap on the amount of Hartree−Fock exchange involved in the exchange correlation functional while Supporting Information, Figure 9B shows a partial MO diagram for the β HOMO−LUMO region for all 14 exchange correlation functionals. When pure DFT methods are used, the β HOMO and LUMO are closer in energy and can interact strongly whereas increasing the amount of Hartree−Fock exchange increases the HOMO−LUMO energy gap and decreases such interaction. For instance, when the BPW91 exchange-correlation functional is used, the β HOMO and LUMO are close in energy ($\Delta E = 0.242$ eV) and can interact with each other to a large extent, decreasing the calculated energy required for electron transfer and forcing electron delocalization. In the case of B3LYP, the β HOMO−LUMO gap increases to 1.876 eV favoring localization (Supporting Information, Figure 10). The HOMO (LUMO) is formed from the interaction of the bonding π (antibonding π^*) orbital of the $C_{ipso}-C_{ipso}$ electron transfer bridge and an out-of-phase (in-phase) $(x^2-y^2)-(x^2-y^2)$ $((x^2-y^2)+(x^2-y^2))$ combination of Fe d orbitals. This increased interaction with π and π^* orbitals of the electron transfer pathway increases the probability of electron transfer. Conversely, B3LYP yields a localized electronic structure conducive to class II behavior, with relatively little interaction between Fe d orbitals and the π and π^* orbitals of the bridge. From Supporting Information, Table 8, both the spin densities and MB parameters follow the same trend with increasing Hartree−Fock exchange.

7.3. H_{ab} Parameter in the BF^+ Cation as a Function of Exchange-Correlation Functional. The dependency on the magnitude of calculated H_{ab} and λ using the B3LYP-xx exchange-correlation functional is shown in Figure 10. The B3LYP-xx approach with 5 to 15% of Hartree−Fock exchange gives delocalized ground states and large H_{ab} values. It is interesting to note the trend in the class III predicted H_{ab} values for Method I as they are almost linear (Supporting Information, Figure 11). This trend also extends

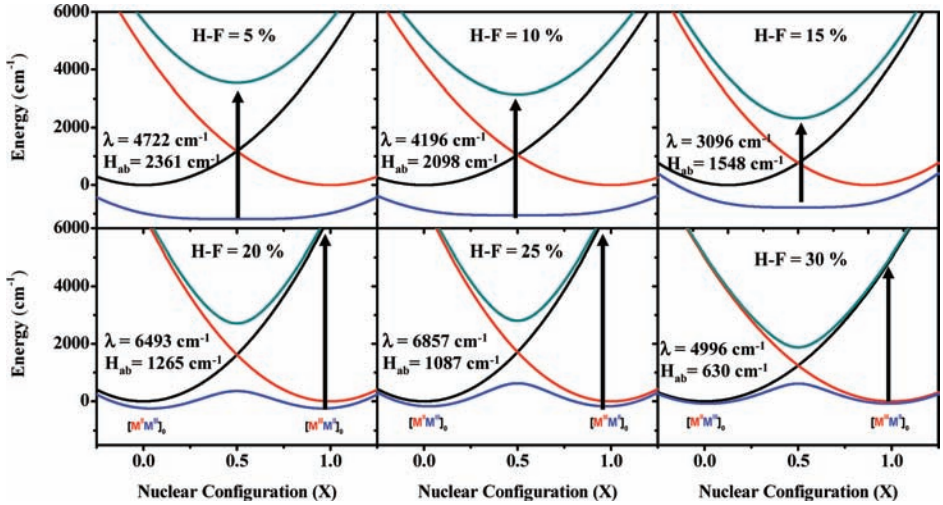

Figure 10. PESs calculated using DFT B3LYP-xx methods with 5, 10, 15, 20, 25, and 30% Hartree−Fock exchange.

to the Class II character predicted for B3LYP-xx method (20−30% of Hartree−Fock exchange)

Conclusion

Density functional theory (DFT) and time-dependent DFT (TDDFT) have been used to explore the potential energy landscapes in the class II (in the Robin and Day classification) MV biferrocene mono-cation (**BF**$^+$) in an effort to evaluate factors affecting optical and thermal intramolecular electron transfer rates. Both energy- and spectroscopy-based benchmarks were used to explore the adiabatic potential energy surfaces (PESs) of the MV **BF**$^+$ cation along with the optimization of appropriate ground-, excited-, and transition-state geometries both in gas phase and in solution. The calculation of Mössbauer isomer shifts and quadrupole splittings, UV−vis excitation energies, and the electronic coupling matrix element, H_{ab}, corroborate the PES analyses. The adiabatic electron transfer pathway is also analyzed with respect to several possible vibronic coordinates. Three methods with which to calculate H_{ab} are explored based on the energies of predicted stationary and transition state geometries coupled with TDDFT calculations. In the best case scenario, we obtain values of 839, 1085, and 1265 cm^{-1} for three different methods used for the evaluation of H_{ab}, respectively, in excellent agreement with experimental data. The degree of the electronic coupling between ferrous and ferric sites, as well as the calculated values of H_{ab} and the nature of the electron transfer pathway, however, correlates with the amount of Hartree−Fock exchange involved in the DFT calculation. In general, the electron transfer pathway involves $Fe^{II}(x^2-y^2)-C_{ipso}(\pi^*)-C_{ipso}(\pi^*)-Fe^{III}(x^2-y^2)$ molecular orbital interactions. To accurately depict factors influencing the electron transfer process in the MV **BF**$^+$ cation, hybrid DFT methods (i.e., B3LYP) can be employed.

Acknowledgment. Generous support from the NSF (CHE-0809203) and Minnesota Supercomputing Institute to V.N.N. is greatly appreciated.

Supporting Information Available: Further details are given in the supporting Figures 1−12 and Tables 1−8. This material is available free of charge via the Internet at http://pubs.acs.org.

IC801801M